

# **Translating pH-sensitive PROgressive saturation for Quantifying Exchange using Saturation Times (PRO-QUEST) MRI to a 3T Clinical Scanner**

Mina Kim<sup>1\*</sup>, Aaron Kujawa<sup>1\*</sup>, Marco Battiston<sup>2</sup>, Eleni Demetriou<sup>1</sup>, Torben Schneider<sup>3</sup>, Sara Collorone<sup>2</sup>, Carmen Tur<sup>2</sup>, Vincent Evans<sup>4</sup>, Sachi Okuchi<sup>1</sup>, David Atkinson<sup>4</sup>, Claudia A.M. Gandini Wheeler-Kingshott<sup>2,5,6</sup>, Xavier Golay<sup>1</sup>

<sup>1</sup> Department of Brain Repair and Rehabilitation, UCL Queen Square Institute of Neurology, Faculty of Brain Sciences, University College London, London, United Kingdom

<sup>2</sup> NMR Research Unit, Queen Square MS Centre, Department of Neuroinflammation, UCL Queen Square Institute of Neurology, Faculty of Brain Sciences, University College London, London, United Kingdom

<sup>3</sup> Philips Healthcare, Surrey, United Kingdom

<sup>4</sup> UCL Centre for Medical Imaging, London, United Kingdom

<sup>5</sup> Department of Brain and Behavioural Sciences, University of Pavia, Pavia, Italy

<sup>6</sup> Brain MRI 3T Research Centre, IRCCS Mondino Foundation, Pavia, Italy

\* Equally contributing authors

**Address correspondence to: Xavier Golay, PhD**

Brain Repair & Rehabilitation

Institute of Neurology

University College London

Email: [x.golay@ucl.ac.uk](mailto:x.golay@ucl.ac.uk)

**Prepared for Submission as a Full paper to *Magnetic Resonance in Medicine***

**Running Head: Translation of pH sensitive MRI to a 3T**

**Keywords:** PRO-QUEST; CEST; clinical 3T MRI; exchange rate; multiple sclerosis

**Word Count: 4925; 5 tables; 5 figures; 37 references**

## **Abstract**

**Purpose:** To translate the recently developed PRO-QUEST (Progressive saturation for quantifying exchange using saturation times) sequence from preclinical 9.4T to 3T clinical magnetic field strength.

**Methods:** Numerical simulations were performed to define the optimal saturation flip angles for PRO-QUEST saturation pulses of at 3T and demonstrate the effect of a  $\Delta T_2$  error on the exchange rate ( $k_{ex}$ ) estimation at various field strengths. Exchange dependent relaxation rate ( $R_{ex}$ ) was measured for glutamate solutions in various pH, healthy volunteers and patients with multiple sclerosis (MS). Additionally, concentration-independent ratiometric  $R_{ex}$  maps were produced to evaluate regional signal variations across the brain of human volunteers.

**Results:** The calculated  $R_{ex}$  significantly correlates with pH in glutamate samples, however  $k_{ex}$  values are underestimated as compared to those previously obtained at 9.4T. In the ratiometric  $R_{ex}$  map of healthy volunteers, no significant differences are found between grey matter, white matter and basal ganglia. In patients with MS, white matter lesions are visible in single saturation power  $R_{ex}$  maps whilst only a periventricular lesion is apparent in the ratiometric  $R_{ex}$  map.

**Conclusion:** We demonstrate that quantification of pH sensitive indices using PRO-QUEST is feasible at 3T within clinically acceptable acquisition times. Our initial findings in patients with MS show that pH sensitive indices varied with the type of lesion examined whilst no significant difference was found in healthy volunteers between tissue types, suggesting that it would be worthwhile to apply PRO-QUEST in a larger cohort of patients to better understand its distinct imaging features relative to conventional techniques.

## Introduction

Understanding pH regulation in the brain is important both in healthy and pathophysiological conditions because tissue acidity may be a key characteristic associated with neurological disorders such as multiple sclerosis (MS), schizophrenia, bipolar disorder, panic attack, ischemia or brain cancer (1-5). In particular, in MS, the neuronal energy deficit, coupled with inflammation, could reduce the cellular pH, leading to acidosis that can induce neuronal degeneration through activation of the acid-sensing ion channel 1A (ASIC) (6). Evidence shows extreme or prolonged acidosis kills neurons whereby ASIC mediates acid-induced toxicity in the central nervous system (7). Conventional MRI methods have failed to detect such subtle pH changes in MS and therefore the ability to non-invasively image pH could be a powerful tool for diagnosis and monitoring of treatment response in MS.

To date, several techniques using MR spectroscopy (MRS) such as  $^{31}\text{P}$  (8,9),  $^{19}\text{F}$  (8,10),  $^1\text{H}$  MRS and MRS imaging (MRSI) (11-13) have been utilised to measure tissue pH. However, their use in clinical practice has been limited by lengthy acquisition times, the need for specialized hardware and/or injection of contrast agents, and poor spatial resolution. Considering the intrinsic limitations of MR spectroscopy in clinical practice, imaging based methodologies have been suggested including contrast enhanced MRI (14) and chemical exchange saturation transfer (CEST) imaging (3,15,16). CEST MRI provides a sensitive detection mechanism that allows characterization of labile protons in contrast to conventional MRI. In particular, amide proton transfer (APT) CEST MRI has been shown to be able to assess ischemic acidosis (3,17), as well as concentration changes on protein and peptides (18,19), which may serve as a surrogate metabolic imaging marker. However, one of the biggest challenges of APT CEST MRI is related to the difficulties of disentangling the proportion of APT signal change caused by protein concentration and pH changes. For example, a recent study by Ray et al. (20) reported that the proportion of APT MRI signal originating from changes in protein concentration was approximately 66% while the remaining 34% originated from changes in tumour pH in a rat model of brain metastasis by combining *in vivo* APT MRI measurements with *ex vivo* histological measurements of protein concentrations. Thus, there is a clear need for non-invasive, reliable quantification of tissue pH in the clinic.

Recently, a novel CEST pulse sequence called PRO-QUEST (Progressive saturation for quantifying exchange using saturation times) has demonstrated the feasibility of estimating pH

sensitive metrics independent of concentration (21), both in phantoms and *in vivo* ischemic rat brains at 9.4T. Here, we aim to translate the PRO-QUEST sequence to a 3T clinical scanner and demonstrate estimation of pH-sensitive indices in phantoms with various pH values and apply the method to assess *in vivo* human neural tissues. In particular, we present here pH-sensitive indices in both healthy brains as well as patients with MS.

## Methods

The PRO-QUEST sequence was originally developed on a 9.4T pre-clinical scanner to reduce the time for measuring chemical exchange rates (21). In this method, an initial saturation pulse sequence is followed by delays (Figure 1A) or off-resonance saturation pulses (Figure 1B) interleaved under non-steady-state conditions while the water magnetization is sampled subsequently through a Look-Locker acquisition until a steady-state magnetization is reached. The Look-Locker sequence (Figure 1A) is used for  $T_1$  measurement, and the resulting  $T_1$  and  $B_1$  parameters (see Data Analysis) are then used as inputs for fitting the signal from the PRO-QUEST sequence (Figure 1B) to estimate the exchange dependent relaxation  $R_{ex}$  and the exchange rate  $k_{ex}$ . Details of the pulse sequence, data acquisition parameters and post-processing procedures are given in the MRI acquisition and data analysis sub-sections.

## Simulation

We performed numerical simulations to investigate the optimal saturation flip angles for the CEST saturation pulse of PRO-QUEST at 3T. Using the MATLAB (The MathWorks, Natick, MA, USA) built-in ordinary differential equation (ODE) solver ode45; the Bloch-McConnell equations were solved for a two-pool system that consisted of one pool describing a glutamate in water solution and the other pool for the water molecules with the following parameters based on previously measured values (21): equilibrium magnetization of water  $M_{0a} = 3000$ , equilibrium magnetization of amine  $M_{0b} = 0.0012M_{0a}$ , longitudinal relaxation time of water  $T_{1a} = 3.2$  s, transversal relaxation time of water  $T_{2a} = 0.25$  s, longitudinal relaxation time of amine  $T_{1b} = 3.2$  s, transversal relaxation time of amine  $T_{2b} = 0.015$  s and  $\Delta\omega_{ba} = 3$  ppm. The model parameters used for the simulations were chosen for relatively high exchange rate in the intermediate exchange regime and wide spectral resolution between glutamate resonance frequency (3 ppm) and the water resonance; this results in a large CEST effect and a moderate influence of direct water saturation. A perfect initial water suppression enhanced through  $T_1$  effects (WET) (22) saturation was assumed by setting the starting values of the x-, y-, z-

components of both pools to 0. For the Look-Locker sequence, the CEST saturation pulse amplitude was set to 0 and the imaging flip angle was set to either 8° or 15°. For the PRO-QUEST sequence, combinations of two flip angles of off-resonance saturation pulses in a range of 63° to 657°, were tested for precise estimation of glutamate exchange rate  $k_{ex}$ . For the simulations, a single PRO-QUEST sequence module consisted of a 20 ms Gaussian-shaped CEST saturation pulse at the glutamate resonance frequency (3 ppm), followed by a 0.5 ms Gaussian-shaped imaging excitation pulse at the water resonance frequency and a 22 ms delay time. This module was repeated 127 times, corresponding to a repetition time of  $TR = 6$  s. A relative  $B_1$ -inhomogeneity of 0.9 was assumed in the simulation. To account for the spoiler gradients, the x- and y-components of both pools were set to 0 after the CEST saturation pulse and after the delay. The simulated transverse magnetization at the end of each readout-pulse corresponds to the measured signal and was obtained by  $M_{xy} = \sqrt{M_x^2 + M_y^2}$ . White Gaussian noise with a standard deviation of  $\sigma = 0.02$  was added to all simulated spectra before the fitting, which was repeated 1000 times with different instances of the noise. Additionally, to verify the applicability of the PRO-QUEST model at 3T compared to high magnetic field strengths (7T and 9.4T), effect of an error  $\Delta T_2$  on  $k_{ex}$  of glutamate ( $k_{ex} = 800$  Hz) was simulated using the same pool and sequence parameters as above.  $\Delta T_2$  errors in the range of -0.1 to 0.1 were added for  $T_{2a} + \Delta T_2$  before estimating  $k_{ex}$ .

### ***Phantom***

Phantoms consisted of 10, 20, 30, 50, 100 mM glutamate (Aldrich-Sigma, Dorset, UK) in a standard solution of 1x phosphate-buffered saline (PBS) with several pH (6.08, 6.64 and 7.19) and a pure PBS sample (pH 7.14). The pH was measured using a micro pH probe (Mettler-Toledo, Columbus OH) and adjusted where necessary with the use of sodium hydroxide and hydrochloric acid. The temperature was kept constant at 20 - 21°C throughout the MRI scans.

### ***Participants***

After local institutional review board approval, 5 healthy volunteers (2 males and 3 females, age range = 27 - 42 years, median = 30) and 2 patients clinically diagnosed with relapsing–remitting MS (RRMS) (2 females, aged 27 and 42 years) provided signed informed consent and underwent brain MRI. The patients with MS were recruited from Queen Square Multiple Sclerosis Centre at the National Hospital of Neurology & Neurosurgery (NHNN) / UCLH Foundation Trust by their attending neurologist. The Expanded Disability Status Scale (EDSS)

(23) was measured within 2 weeks of the MRI examination (EDSS = 2.0 and 3.0 for MS patient 1 and 2, respectively).

### ***MRI Acquisition***

All images were acquired using a 3T Philips Ingenia CX MRI scanner (Philips Healthcare, Best, the Netherlands). Phantoms and healthy volunteers were scanned using a 32-channel head coil. The second-order shims were optimised to minimise  $B_0$  field inhomogeneity.

A set of measurement consisted of 1) 1<sup>st</sup> Look-Locker scan with a readout flip angle  $\theta_1$ , 2) 2<sup>nd</sup> Look-Locker scan with a readout flip angle  $\theta_2$ , 3) 1<sup>st</sup> PRO-QUEST scan with a high power saturation pulse with a readout flip angle  $\theta_1$ , 4) 2<sup>nd</sup> PRO-QUEST scan with a low power saturation pulse a readout flip angle  $\theta_1$  and 5) quantitative  $T_2$  scan. A Look-Locker sequence (Figure 1A) was implemented with 20 ms delay time prior to a fast gradient echo readout (EPI factor = 7) and multiple acquisitions (128 for a phantom and 143 for volunteers) with the following imaging parameters: imaging readout excitation pulse = sinc-gaussian (1 period of oscillation, symmetrically centred), duration = 0.67 ms, flip angle of readout pulse  $\theta_1 = 8^\circ$  for the first Look-Locker scan and  $\theta_2 = 15^\circ$  for the second Look-Locker scan, TE = 3.8 ms,  $\tau$  duration (time between readout pulses) = 42 ms, acquired resolution =  $1.88 \times 2.14 \times 5 \text{ mm}^3$  (phantom) and  $1.96 \times 2.04 \times 5 \text{ mm}^3$  (volunteers), TR = 6 s, SENSE acceleration factor = 2. For the PRO-QUEST scans (Figure 1B), an off-resonance saturation pulse centred at 3.0 ppm (glutamate phantom) or 3.5 ppm (volunteers) was applied prior to the turbo-field echo-planar imaging (TFEPI) readouts with identical imaging parameters as the Look-Locker sequence. Parameters for the off-resonance saturation pulses used in the PRO-QUEST sequence are as follows: off-resonance saturation pulse = sinc-gaussian (3 periods of oscillation, symmetrically centred), bandwidth = 300 Hz, duration = 20ms, flip angle of the 1<sup>st</sup> PRO-QUEST scan =  $450^\circ$  (equivalent of 1.47  $\mu\text{T}$  peak amplitude), flip angle of the 2<sup>nd</sup> PRO-QUEST scan =  $250^\circ$  (equivalent of 0.82  $\mu\text{T}$  peak amplitude), flip angle of readout pulse =  $8^\circ$ . For the phantom scan, 3 slices in axial orientation were obtained with 1 average which resulted in a scan time of 2 min 30 s per sequence. For the volunteer brain scans, an axial single slice was acquired with 3 averages to improve signal to noise ratio for a scan time of 2 min 6 s per sequence. Finally, standard multi-echo Carr-Purcell-Meiboom-Gill (CPMG) sequence consisting of 10 echoes with TE = 20-200 ms with 20 ms of inter-echo spacing was used to quantify  $T_2$  in the same

geometry as the Look-Locker and the PRO-QUEST scans. The total scan time for the *in vivo* protocol was 9 min 48 sec. The Imaging parameters for this study are summarised in Table 1.

For patients with MS, an additional Phase-Sensitive Inversion-Recovery (PSIR) scan was performed using TSE sequence as a clinical examination routine with the following parameters: nominal resolution = 0.5 x 0.5 x 2 mm<sup>3</sup>, 75 axial slices, TE = 13 ms, TR = 11329 ms, TI = 400 ms, TSE factor = 8, refocusing flip angle = 120°. For patient 1, PRO-QUEST sequence was performed at two separate axial locations whilst a single slice was obtained for patient 2.

### **Data Analysis**

Data processing was performed using custom-written scripts in MATLAB (The Mathworks, Natick, MA, USA). The Bloch-McConnell models were re-derived in a similar way to the previous study (21), but took the first delay time ( $\tau$ ) into account (derivation described in Supporting Information) contrary to that previous study. Then the derived models were fitted to magnitude data using maximum likelihood estimation. The following equation describes the magnetization at the  $N$ th readout and was fitted to the Look-Locker data to estimate the equilibrium magnetization  $M_0$  and  $T_1$ :

$$M(t = t_d + (N - 1)\tau + t_{del}) = [M_0(1 - e^{-t_d R_1})e^{-t_{del} R_1} + M_0(1 - e^{-t_{del} R_1})](\cos \theta)e^{-\tau R_1})^{N-1} + M_{zd}(\tau) \frac{1 - ((\cos \theta)e^{-\tau R_1})^{(N-1)}}{1 - (\cos \theta)e^{-\tau R_1}} \quad [1]$$

where  $M_{zd}(\tau) = M_0 (1 - e^{-\tau R_1})$ ;  $t_d$  is the time between the initial saturation pulse and the first readout pulse;  $\tau$  is the time between readout pulses with small flip angle  $\theta$ ;  $R_1 = 1/T_1$ ;  $t_{del}$  is the delay time replacing the CEST saturation pulse. In order to account for  $B_1$  inhomogeneity, only  $\theta$  was assumed to be proportional to  $B_1$  in equation 1:

$$\theta \rightarrow \frac{B_{1,act}}{B_{1,nom}} \theta, \quad [2]$$

where  $B_{1,act}$  and  $B_{1,nom}$  are the actual and nominal RF field strength, respectively.  $B_1$  (i.e.,  $B_{1,act}$ ) is obtained by simultaneously fitting two Look-Locker data sets acquired at different  $B_{1,nom}$  using equation.

Next, the obtained  $M_0$ ,  $T_1$ ,  $B_1$  values were used as input parameters for estimating the exchange-dependent relaxation,  $R_{ex}$  by fitting the PRO-QUEST data (derivation in Supporting Information):

$$\begin{aligned}
M(t = t_d + (N - 1)\tau + t_{\text{sat}}) &= [M_0(1 - e^{-t_d R_1})e^{-t_{\text{sat}} R_1 \rho} + M_{\text{SS}}(1 - e^{-t_{\text{sat}} R_1 \rho})]((\cos \theta)e^{-t_{\text{sat}} R_1 \rho} e^{-(\tau - t_{\text{sat}}) R_1})^{(N-1)} \\
&+ M_{\text{zsat}}(\tau) \left( \frac{1 - ((\cos \theta)e^{-t_{\text{sat}} R_1 \rho} e^{-(\tau - t_{\text{sat}}) R_1})^{(N-1)}}{1 - ((\cos \theta)e^{-t_{\text{sat}} R_1 \rho} e^{-(\tau - t_{\text{sat}}) R_1})} \right)
\end{aligned} \tag{3}$$

where  $M_{\text{zsat}}(\tau) = M_0(1 - e^{-(\tau - t_{\text{sat}}) R_1})e^{-t_{\text{sat}} R_1 \rho} + M_{\text{SS}}(1 - e^{-t_{\text{sat}} R_1 \rho})$  and  $M_{\text{SS}} = \frac{R_1 \cos \varphi}{R_{1\rho}}$  is the steady-state magnetization;  $R_{1\rho} = R_1(\cos \varphi)^2 + R_2(\sin \varphi)^2 + R_{\text{ex}}$  is the relaxation constant along the effective field;  $t_{\text{sat}}$  is the time for the CEST saturation pulse;  $\varphi$  is the angle between the effective irradiation field and the z-axis.

The exchange-dependent relaxation  $R_{\text{ex}}$  that induces the CEST effect can be described as

$$R_{\text{ex}} = \frac{\rho_B \delta^2 k_{\text{ex}}}{((\delta - \Omega)^2 + \omega_1^2 + k_{\text{ex}}^2)} (\sin \varphi)^2 \tag{4}$$

where  $\cos \varphi = \frac{\Omega}{\sqrt{\omega_1^2 + \Omega^2}}$  and  $\varphi$  is the angle between the effective field and the z-axis;  $\rho_B$  is fractional concentration of the labile exchangeable protons;  $\delta$  is Larmor frequency of the exchangeable labile protons;  $\Omega$  is frequency offset with respect to water;  $\omega_1$  is angular frequency for low amplitude of the RF field.

Concentration-independent ratiometric  $R_{\text{ex}}$  can be calculated as  $R_{\text{ex,low}}/R_{\text{ex,high}}$  as follows:

$$\text{Ratiometric } R_{\text{ex}} = \frac{R_{\text{ex,low}}}{R_{\text{ex,high}}} = \frac{((\delta - \Omega)^2 + \omega_2^2 + k_{\text{ex}}^2)}{((\delta - \Omega)^2 + \omega_1^2 + k_{\text{ex}}^2)} \tag{5}$$

where  $\omega_2$  is angular frequency for high amplitude of the RF field;  $R_{\text{ex,low}}$  is the exchange dependent relaxation by PRO-QUEST scan with a low power saturation pulse;  $R_{\text{ex,high}}$  is the exchange dependent relaxation by PRO-QUEST scan with a high power saturation pulse.

Regions of interest (ROI) were manually drawn in anatomical regions and defined as white matter (WM: frontal lobe, occipital lobe, genu and splenium of corpus callosum), grey matter (GM: frontal lobe, occipital lobe), basal ganglia (caudate, putamen) and thalamus. Firstly, ROIs of approximately equal size were placed in 9 different positions for each volunteer and average of  $T_1$  values among all volunteers for each ROI was calculated to be compared to literature values. Subsequently, ROIs were grouped into 4 tissue types (WM, GM, basal ganglia and thalamus) and average of the ratiometric  $R_{\text{ex}}$  values in each tissue type was computed for each volunteer. Mixed effects model was used to evaluate statistical significance for ratiometric  $R_{\text{ex}}$

differences of each pair combination (in total 6 pairs) by taking into account 5 volunteers and 4 tissue types in STATA 13 (StataCorp., 2013).

## Results

Figure 2 shows each pair of flip angles for PRO-QUEST saturation pulses that match with a specific exchange rate  $k_{ex}$ . Our simulated results indicate that a combination of minimum flip angle of  $300^\circ$  for the 1<sup>st</sup> PRO-QUEST sequence and  $630^\circ$  for the 2<sup>nd</sup> PRO-QUEST sequence is optimal to precisely estimate  $k_{ex}$  of glutamate (800 Hz) with additive noise (Figure 2A and 2B). A standard deviation of the added noise was  $0.005M_{0a}$  for the Look-Locker and PRO-QUEST data and  $0.005T_{2a}$  for  $T_2$  data. Nevertheless, the maximum flip angles combination for PRO-QUEST saturation pulses available at 3T scanner were  $250^\circ$  and  $450^\circ$  due to specific absorption rate (SAR) limitations. Additional simulations (Figure 2C) show that the effect of an error  $\Delta T_2$  of water on  $k_{ex}$  is much larger at 3T compared to higher magnetic field strength (7T and 9.4T).

Similar to the pre-clinical case (21), progressive saturation recovery curves with off-resonance saturation pulses show clear separation among samples with various pH values in glutamate of 100 mM and PBS (Figure 3B and 3C) while the ones without off-resonance saturation pulses are nearly indistinguishable (Figure 3A and 3C). This is reproducible at much lower concentration of 20 mM glutamate samples with various pH (Supporting Information Figure S1A and S1B). It is also seen that PRO-QUEST saturation recovery curves are independent of glutamate concentration with the PRO-QUEST pulse (Supporting Information Figure S1C and S1D). The corresponding mean values of single power  $R_{ex}$  ( $R_{ex,high}$ ) and ratiometric  $R_{ex}$  significantly correlate with pH in glutamate samples (Figure 3 and Supporting Information Figure S2B). Mean ratiometric  $R_{ex}$  value at a fixed pH of 6.08 ranged from 0.52 to 0.56, which is not significantly different between various concentration of glutamate samples (Supporting Information Figure S2C). This confirms the concentration independence of the ratiometric  $R_{ex}$  maps, whereas mean ratiometric  $R_{ex}$  value is significantly changed at various pH with a fixed concentration of glutamate samples (20 mM) (Supporting Information Figure S2D).  $k_{ex}$  values are underestimated as compared to those estimated at 9.4T in the previous study (Table 2) (21).

In healthy volunteers, the PRO-QUEST image of signal evolution at the final sampling point and the corresponding saturation recovery curves show clear contrast between WM, GM and cerebrospinal fluid (CSF) (Figure 4B and 4E) contrary to the Look-Locker image (Figure 4A)

and the corresponding saturation recovery curves (without off-resonance saturation pulses) (Figure 4D), which is primarily based on water content  $M_0$ . This confirms the effect of progressive CEST pulses and magnetisation transfer (MT). As for prerequisite in parameters estimation of PRO-QUEST indices, average  $T_1$  values from the Look-Locker scan in 5 healthy volunteers are consistent with literature values (Table 3) (24-26). The  $B_1$  map (in % of the nominal angle) obtained from the same volunteer shows severe  $B_1$  inhomogeneity in the centre of the ventral brain near the thalamus (Figure 4F).  $R_{ex}$  maps at single power saturation pulse show signal variations across the brain which are likely to be affected by the concentration of macromolecules (e.g. hyaluronic acid and chondroitin sulphate) (27) independently of pH. On the other hand, in the ratiometric analysis, contribution of macromolecular concentrations is cancelled out as shown in equation 5 and therefore the ratiometric  $R_{ex}$  is expected to be specific to pH changes. To this end, it is reasonable to expect that a ratiometric  $R_{ex}$  (i.e., a metric of  $R_{ex,low}$  divided by  $R_{ex,high}$ ) may produce a concentration-independent  $R_{ex}$ . In the ratiometric  $R_{ex}$  map of healthy volunteers, no significant differences are found between GM, WM and basal ganglia (Figure 4I) while regional variations across the brain are displayed in both  $R_{ex}$  maps of low (Figure 4G) and high saturation power (Figure 4H). Significant difference in ratiometric  $R_{ex}$  maps was found only between WM and Thalamus ( $p < 0.05$ ) (Table 4).

Figure 5A shows three slices from two different MS patients presenting with heterogeneous MS lesions. Progressive saturation recovery curves with off-resonance saturation pulses show clear separation between normal appearing white matter (NAWM) and all MS lesions (Figure 5B and 5C). In patient 1, a non-confluent periventricular lesion adjacent to the posterior horn of the lateral ventricles was observed in all  $R_{ex}$  maps consistent with  $T_1w$ . Moreover, no hypointense areas were visible in the temporal lobe and thalamus in the ratiometric  $R_{ex}$  map. Averaged ratiometric  $R_{ex}$  of the periventricular lesion (lesion 1) and WM lesion (lesion 3) were 0.56 and 0.52, respectively, whereas both NAWM and juxtacortical lesion (lesion 2) presented 0.48 (Table 5). In patient 2, hypointense WM lesions were observed in the temporal lobe (lesion 4) and occipital lobe (lesion 5) in  $T_1w$  PSIR,  $R_{ex,low}$  and  $R_{ex,high}$  whilst those lesions did not appear in the ratiometric  $R_{ex}$  map (Figure 5A). Averaged ratiometric  $R_{ex}$  of both lesions (L4 and L5) and NAWM were 0.48 and 0.49, respectively (Table 5).

## Discussion

APT signal is known to be sensitive to the pH of tissue, which is heavily dependent on the exchange rate of amide protons with solvent water protons (3). Previous studies have reported

that APT-CEST can detect alterations in cerebral pH in ischemic animal models (3,17). However, decoding the different elements contributing to APT signal has not been trivial as it also relies on protein concentration in addition to pH and temperature. Here, we aimed to translate a new MR imaging method sensitive to tissue pH which was previously demonstrated in a preclinical system 9.4T (PRO-QUEST) (21) to a 3T clinical system, and report features of the pH dependent metrics in pH phantoms, healthy subjects and patients with MS. Several acquisition methods have been developed to measure exchange rates or pH (16,28-30) prior to PRO-QUEST. The observant reader will notice that the PRO-QUEST sequence resembles the multi-echo Length and Offset VARied Saturation (MeLOVARS) method, as both methods are based on Look-Locker types of acquisition. However, as shown in Figure 1, PRO-QUEST utilizes a WET pulse preparation to set the initial magnetization value and allow observation of a  $T_1$  recovery curve to describe a whole system, whereas MeLOVARS deliberately samples outside the steady-state to observe a build-up of saturation. This unique characteristic of PRO-QUEST allows calculation of exchange-dependent relaxation which can be advantageous to determine pH-independent metrics.

In this study, we have tested phantoms with glutamate which is one of the most abundant amino acids in the human brain. However, it is noteworthy that saturation recovery curves obtained from the phantom are not ‘calibration curves’ representing the effect *in vivo*, and therefore they would certainly not reflect on the whole exchangeable protons present in the brain. Our phantom results demonstrate that the ratiometric  $R_{ex}$  significantly correlates with pH (Figure 3E) and is independent of sample concentration (Supporting Information Figure S2), whilst the metric  $k_{ex}$  is found to be underestimated as compared to those measured at 9.4T (Table 2). An underestimation of  $k_{ex}$  is attributed to an underestimation of the measured relaxation times  $T_1$  and  $T_2$  of the solutions with the CEST agent due to chemical exchange, while leaving the intrinsic relaxation rates of the water pool  $T_{1a}$  and  $T_{2a}$  unaffected (i.e.,  $T_1 \neq T_{1a}$  and  $T_2 \neq T_{2a}$ ). Previous studies reported that  $T_1$  was underestimated compared to  $T_{1a}$  in inversion recovery (IR) experiments (31) and the effect on  $T_2$  measured with a spin-echo based CPMG sequence was even greater (32) due to the effect of chemical exchange on the measured relaxation times. In particular, the measured  $T_2$  is shown to depend on the time delay between the spin echoes. Only for small time delays compared to the mean exchange lifetime, the exchange effect can be neglected (i.e.,  $T_2 \approx T_{2a}$ ). For exchange rates in the order of  $10^3$  Hz, the delay times would have to be shorter than 2 ms, which is not feasible on clinical scanners. Our simulated data

(Figure 3C) illustrates that the dependence of  $R_{ex}$  on  $T_2$  errors significantly increases at clinical field strength. The spin echo sequence applied in the present study to determine  $T_2$  had delay times much greater than the mean exchange lifetime, such that the measured  $T_2$  becomes significantly shorter than  $T_{2a}$ . This leads to an overestimation of the exchange-independent relaxation rate  $R_{eff}$  (analogous to the spillover overestimation in a Z-spectrum). To this end, such broader direct saturation effect mediated by  $R_2$  at clinical field strength ( $R_2$  effects  $\gg R_{ex}$  effects) results in underestimating  $k_{ex}$ , and therefore the presented pH-weighted images are likely to suffer from that field-dependent bias. As such, the PRO-QUEST method, while it increases the precision over other pH-assessing methods, does not improve their accuracy.

Averaged  $T_1$  values of 5 healthy volunteers estimated from the Look-Locker scan are consistent with literature values, although there are areas where  $T_1$  lies towards the high-end range as compared to previously reported values at 3T (Table 3) (25,26,33). This can be explained by variation on the choice of ROIs, spatial resolution (e.g., partial volume effects in GM) and the pulse sequences used for measurement (e.g., use of IR instead of Look-Locker).

While the  $R_{ex}$  metrics produced from each single power PRO-QUEST sequence show regional signal variations, to date, no significant differences in intracellular pH between GM and WM have previously been found in healthy brains using  $^{31}\text{P}$  NMR techniques (34). Therefore it is crucial to evaluate the origin of the measured imaging signal and its association with tissue pH. In this study, assessment of  $R_{ex}$  is achieved independently of the amount of substrate through the use of two different saturation powers. The ratio of these two measurements provides a concentration-independent metric  $R_{ex}$  as signal changes are only related to pH or temperature. Whilst the temperature in the brain is expected to stay constant, the changes seen can be directly attributed to pH changes.

We investigated regional variations in ratiometric  $R_{ex}$  metrics across the brain and found no significant differences in signal between structurally distinct brain regions except between WM and the Thalamus ( $p < 0.05$ ) (Table 4), which might likely be accounted for by imperfect  $B_1$  correction in the centre of the ventral brain near the thalamus. In a 2D acquisition, the effective flip angle for shaped RF pulses such as gaussian pulses used in this study depends on the slice profile which needs to be considered in estimating the flip angle correction factor (21). On the other hand, in a 3D acquisition scheme, the flip angle discrepancy is mainly due to  $B_1$  effect and therefore reflects  $B_1$  inhomogeneity independent of the slice profile. As the PRO-QUEST

method is particularly sensitive to  $B_1$  inhomogeneities, development of a fast 3D PRO-QUEST sequence would be able to improve estimation of  $B_1$ .

Our results illustrate clear separation between NAWM and all MS lesions in progressive saturation recovery curves with off-resonance saturation pulses (Figure 5B and 5C). The separation between these curves arises primarily from different  $T_1$  values within the ROIs, whereas other effects such as various concentrations in metabolites or proteins may play an additional role. Furthermore, we show that, while WM lesions visible on single power  $R_{ex}$  maps are consistent with  $T_{1w}$  images, only one periventricular lesion is visible on the ratiometric  $R_{ex}$  map (Figure 5A, Table 5). Typically, patients with MS present with various lesion types due to a diverse pathophysiology. Studies suggest that such periventricular lesions perpendicular to the ventricle are the results of inflammation around penetrating venules and there is a predominantly perivenous demyelination in non-confluent periventricular lesions (35). Here, we present only two MS patients for demonstration of applicability of PRO-QUEST at clinical field strength and therefore we hope that a further investigation will uncover the potentials of this new method applied to MS for aiding in the discrimination of lesion type.

It is worth noting that there are a few limitations to the present study. The first limitation is the use of single-slice readout which was designed to ensure a clinically acceptable scan time. This leads to challenges for motion correction that is essential for data acquired on the time scale of CEST MRI (36) whilst noticeable head motions were not observed in the human data obtained in this study. As such, further development of a 3D PRO-QUEST sequence within clinically acceptable scan time is required. Second, the PRO-QUEST method with single irradiation frequency might be susceptible to  $B_0$  shifts. As the previous pre-clinical study reported, this could be mitigated by using broad bandwidth saturation pulses (21). A bandwidth of 300 Hz was used in the present study in consideration of the  $B_0$  effect. Additional work is necessary to validate the multiple irradiation frequencies of PRO-QUEST as an adequate reference and to study their sensitivity and specificity compared to the analysis regimen presented here. Another limitation is the effect of MT and small  $R_{ex}$  with comparison to large  $R_2$  effects at 3T. A few approaches exist to correct for the effect of direct saturation and MT in Z-spectra, such as the MTR-asymmetry ( $MTR_{asym}$ ) approach (3) and the 3-point method (37). However, they are not applicable to the present study as  $MTR_{asym}$  relies on the assumption that the reference points are affected solely by symmetric contributions with respect to the water peak and the 3-point method assumes a linear relationship between the effect size of confounding contributions and

the frequency offset of the CEST pulse, which may not properly correct for the presence of other CEST pools. Finally, due to intrinsic limitations of the SAR and duty cycle (50%) at clinical field strength, the efficiency of the off-resonance saturation scheme is somewhat compromised. Nonetheless, clinical translation of this technique is feasible given its easy implementation on standard clinical platforms and the use of existing Look-Locker type of readouts, therefore not requiring pulse programming.

## **Conclusion**

In this study, we demonstrated that it is feasible to estimate a pH sensitive metric using PRO-QUEST at 3T within clinical acquisition times (around 10 min.) with minimum pulse programming. Whilst exchange rate ( $k_{ex}$ ) is found to be underestimated due to the larger direct saturation effect at clinical field strengths, exchange dependent relaxation  $R_{ex}$  metric shows significant correlation with pH in phantoms. Furthermore, no significant differences were observed in ratiometric  $R_{ex}$  metric (a ratio between  $R_{ex,high}$  and  $R_{ex,low}$ ) between GM and WM in healthy brains as ratiometric  $R_{ex}$  is expected to be a concentration-independent and pH-sensitive metric. Our initial findings in patients with MS suggest that it would be worthwhile to apply PRO-QUEST in larger cohort studies on patients with neurological impairment to better understand its distinct imaging features relative to conventional techniques.

**Acknowledgements:** This work was supported in parts by funding from the National Institute for Health Research (NIHR) University College London Hospitals Biomedical Research Centre (UCLH BRC), and from the European Union's Horizon 2020 research and innovation programme under the Grant Agreement No 667510 (support to M.K., E.D., X.G.). A Kujawa was supported by Olea Medical® and the EPSRC-funded UCL Centre for Doctoral Training in Medical Imaging (EP/L016478/1). M Kim is supported by the Multiple Sclerosis Society Innovative Grant.

## References

1. Esquivel G, Schruers KR, Maddock RJ, Colasanti A, Griez EJ. Acids in the brain: a factor in panic? *J Psychopharmacol* 2010;24(5):639-647.
2. Dogan AE, Yuksel C, Du F, Chouinard VA, Ongur D. Brain lactate and pH in schizophrenia and bipolar disorder: a systematic review of findings from magnetic resonance studies. *Neuropsychopharmacology* 2018;43(8):1681-1690.
3. Zhou J, Payen JF, Wilson DA, Traystman RJ, van Zijl PC. Using the amide proton signals of intracellular proteins and peptides to detect pH effects in MRI. *Nature medicine* 2003;9(8):1085-1090.
4. Gillies RJ, Raghunand N, Garcia-Martin ML, Gatenby RA. pH imaging. A review of pH measurement methods and applications in cancers. *IEEE Eng Med Biol Mag* 2004;23(5):57-64.
5. Ciccarelli O, Barkhof F, Bodini B, De Stefano N, Golay X, Nicolay K, Pelletier D, Pouwels PJ, Smith SA, Wheeler-Kingshott CA, Stankoff B, Yousry T, Miller DH. Pathogenesis of multiple sclerosis: insights from molecular and metabolic imaging. *Lancet Neurol* 2014;13(8):807-822.
6. Friese MA, Craner MJ, Etzensperger R, Vergo S, Wemmie JA, Welsh MJ, Vincent A, Fugger L. Acid-sensing ion channel-1 contributes to axonal degeneration in autoimmune inflammation of the central nervous system. *Nature medicine* 2007;13(12):1483-1489.
7. Wemmie JA, Taugher RJ, Kreple CJ. Acid-sensing ion channels in pain and disease. *Nat Rev Neurosci* 2013;14(7):461-471.
8. Ojugo AS, McSheehy PM, McIntyre DJ, McCoy C, Stubbs M, Leach MO, Judson IR, Griffiths JR. Measurement of the extracellular pH of solid tumours in mice by magnetic resonance spectroscopy: a comparison of exogenous (19)F and (31)P probes. *NMR Biomed* 1999;12(8):495-504.
9. Gillies RJ, Liu Z, Bhujwala Z. 31P-MRS measurements of extracellular pH of tumors using 3-aminopropylphosphonate. *Am J Physiol* 1994;267(1 Pt 1):C195-203.
10. McSheehy PM, Seymour MT, Ojugo AS, Rodrigues LM, Leach MO, Judson IR, Griffiths JR. A pharmacokinetic and pharmacodynamic study in vivo of human HT29 tumours using 19F and 31P magnetic resonance spectroscopy. *Eur J Cancer* 1997;33(14):2418-2427.
11. van Sluis R, Bhujwala ZM, Raghunand N, Ballesteros P, Alvarez J, Cerdan S, Galons JP, Gillies RJ. In vivo imaging of extracellular pH using 1H MRSI. *Magn Reson Med* 1999;41(4):743-750.
12. Garcia-Martin ML, Herigault G, Remy C, Farion R, Ballesteros P, Coles JA, Cerdan S, Ziegler A. Mapping extracellular pH in rat brain gliomas in vivo by 1H magnetic resonance spectroscopic imaging: comparison with maps of metabolites. *Cancer Res* 2001;61(17):6524-6531.
13. Bhujwala ZM, Artemov D, Ballesteros P, Cerdan S, Gillies RJ, Solaiyappan M. Combined vascular and extracellular pH imaging of solid tumors. *NMR Biomed* 2002;15(2):114-119.
14. Raghunand N, Howison C, Sherry AD, Zhang S, Gillies RJ. Renal and systemic pH imaging by contrast-enhanced MRI. *Magn Reson Med* 2003;49(2):249-257.
15. Longo DL, Bartoli A, Consolino L, Bardini P, Arena F, Schwaiger M, Aime S. In Vivo Imaging of Tumor Metabolism and Acidosis by Combining PET and MRI-CEST pH Imaging. *Cancer Res* 2016;76(22):6463-6470.

16. McMahon MT, Gilad AA, Zhou J, Sun PZ, Bulte JW, van Zijl PC. Quantifying exchange rates in chemical exchange saturation transfer agents using the saturation time and saturation power dependencies of the magnetization transfer effect on the magnetic resonance imaging signal (QUEST and QUESP): Ph calibration for poly-L-lysine and a starburst dendrimer. *Magn Reson Med* 2006;55(4):836-847.
17. Sun PZ, Zhou J, Sun W, Huang J, van Zijl PC. Detection of the ischemic penumbra using pH-weighted MRI. *J Cereb Blood Flow Metab* 2007;27(6):1129-1136.
18. Zhou J, Lal B, Wilson DA, Laterra J, van Zijl PC. Amide proton transfer (APT) contrast for imaging of brain tumors. *Magn Reson Med* 2003;50(6):1120-1126.
19. Jones CK, Schlosser MJ, van Zijl PC, Pomper MG, Golay X, Zhou J. Amide proton transfer imaging of human brain tumors at 3T. *Magn Reson Med* 2006;56(3):585-592.
20. Ray KJ, Simard MA, Larkin JR, Coates J, Kinchesh P, Smart SC, Higgins GS, Chappell MA, Sibson NR. Tumor pH and Protein Concentration Contribute to the Signal of Amide Proton Transfer Magnetic Resonance Imaging. *Cancer Res* 2019;79(7):1343-1352.
21. Demetriou E, Tachrount M, Zaiss M, Shmueli K, Golay X. PRO-QUEST: a rapid assessment method based on progressive saturation for quantifying exchange rates using saturation times in CEST. *Magn Reson Med* 2018;80(4):1638-1654.
22. Ogg RJ, Kingsley PB, Taylor JS. WET, a T1- and B1-insensitive water-suppression method for in vivo localized 1H NMR spectroscopy. *J Magn Reson B* 1994;104(1):1-10.
23. Kurtzke JF. Rating neurologic impairment in multiple sclerosis: an expanded disability status scale (EDSS). *Neurology* 1983;33(11):1444-1452.
24. Wansapura JP, Holland SK, Dunn RS, Ball WS. NMR relaxation times in the human brain at 3.0 Tesla. *J Magn Reson Imaging* 1999;9:531-538.
25. Gelman N, Ewing JR, Gorell JM, Spickler EM, Solomon EG. Interregional variation of longitudinal relaxation rates in human brain at 3.0 T: relation to estimated iron and water contents. *Magn Reson Med* 2001;45(1):71-79.
26. Lu H, Nagae-Poetscher LM, Golay X, Lin D, Pomper M, van Zijl PC. Routine clinical brain MRI sequences for use at 3.0 Tesla. *J Magn Reson Imaging* 2005;22(1):13-22.
27. Kilia V, Skandalis SS, Theocharis AD, Theocharis DA, Karamanos NK, Papageorgakopoulou N. Glycosaminoglycan in cerebrum, cerebellum and brainstem of young sheep brain with particular reference to compositional and structural variations of chondroitin-dermatan sulfate and hyaluronan. *Biomed Chromatogr* 2008;22(9):931-938.
28. Longo DL, Dastru W, Digilio G, Keupp J, Langereis S, Lanzardo S, Prestigio S, Steinbach O, Terreno E, Uggeri F, Aime S. Iopamidol as a responsive MRI-chemical exchange saturation transfer contrast agent for pH mapping of kidneys: In vivo studies in mice at 7 T. *Magn Reson Med* 2011;65(1):202-211.
29. Chen LQ, Howison CM, Jeffery JJ, Robey IF, Kuo PH, Pagel MD. Evaluations of extracellular pH within in vivo tumors using acidoCEST MRI. *Magn Reson Med* 2014;72(5):1408-1417.
30. Song X, Xu J, Xia S, Yadav NN, Lal B, Laterra J, Bulte JW, van Zijl PC, McMahon MT. Multi-echo length and offset VARied saturation (MeLOVARS) method for improved CEST imaging. *Magn Reson Med* 2015;73(2):488-496.
31. Spencer RG, Fishbein KW. Measurement of spin-lattice relaxation times and concentrations in systems with chemical exchange using the one-pulse sequence: breakdown of the Ernst model for partial saturation in nuclear magnetic resonance spectroscopy. *J Magn Reson* 2000;142(1):120-135.

32. Fabri D, Williams MA, Halstead TK. Water T2 relaxation in sugar solutions. *Carbohydr Res* 2005;340(5):889-905.
33. Wansapura JP, Holland SK, Dunn RS, Ball WS, Jr. NMR relaxation times in the human brain at 3.0 tesla. *J Magn Reson Imaging* 1999;9(4):531-538.
34. Mason GF, Chu WJ, Vaughan JT, Ponder SL, Twieg DB, Adams D, Hetherington HP. Evaluation of <sup>31</sup>P metabolite differences in human cerebral gray and white matter. *Magn Reson Med* 1998;39(3):346-353.
35. Adams CW, Abdulla YH, Torres EM, Poston RN. Periventricular lesions in multiple sclerosis: their perivenous origin and relationship to granular ependymitis. *Neuropathol Appl Neurobiol* 1987;13(2):141-152.
36. Zaiss M, Herz K, Deshmane A, Kim M, Golay X, Lindig T, Bender B, Ernemann U, Scheffler K. Possible artifacts in dynamic CEST MRI due to motion and field alterations. *J Magn Reson* 2019;298:16-22.
37. Jin T, Wang P, Zong X, Kim SG. MR imaging of the amide-proton transfer effect and the pH-insensitive nuclear overhauser effect at 9.4 T. *Magn Reson Med* 2013;69(3):760-770.

## Table Legends

Table 1. Imaging parameters utilised in this study. Note that offset frequency was applied to only PRO-QUEST scans.

	Pre-saturation (CEST) pulse			Readout pulse		Scan Time (minutes: seconds)	
	Duration (ms)	Flip Angle (deg)	Offset frequency (ppm)	Flip Angle (deg)	Acquisition	1 NEX (3D)	3 NEX (2D)
1 <sup>st</sup> Look-Locker	-	-	-	8	3D or 2D FFE with TFEPI	2:30	2:06
2 <sup>nd</sup> Look-Locker	-	-	-	15	3D or 2D FFE with TFEPI	2:30	2:06
1 <sup>st</sup> PRO-QUEST *	20	450	3 <sup>†</sup> or 3.5 <sup>††</sup>	8	3D or 2D FFE with TFEPI	2:30	2:06
2 <sup>nd</sup> PRO-QUEST **	20	250	3 <sup>†</sup> or 3.5 <sup>††</sup>	8	3D or 2D FFE with TFEPI	2:30	2:06

\* Equivalent of 1.47  $\mu$ T peak amplitude

\*\* Equivalent of 0.82  $\mu$ T peak amplitude

<sup>†</sup> For Glutamate phantoms

<sup>††</sup> For Human brain

Table 2.  $k_{ex}$  values ( $\times 10^3 \text{ s}^{-1}$ ) of the present study in glutamate phantoms (3T) as compared to literature (9.4T).

	pH		
	6.1	6.6	7.2
Present Study	$0.56 \pm 0.02$	$0.65 \pm 0.04$	$0.68 \pm 0.04$
Study <sup>a</sup>	$0.71 \pm 0.03$	$0.84 \pm 0.03$	$1.27 \pm 0.20$
Study <sup>b</sup>	$0.72 \pm 0.22$	$1.04 \pm 0.19$	$1.66 \pm 0.28$

<sup>a</sup>Demetriou et al. (21): PRO-QUEST

<sup>b</sup>Demetriou et al. (21): QUEST

Table 3. Absolute T<sub>1</sub> relaxation times of the present study in healthy brains as compared to literature. ROIs are displayed in Figure 4C. FWM = frontal white matter; OWM = occipital white matter; CC = corpus callosum; FGM = frontal grey matter; OGM = occipital grey matter.

	Present Study	Study <sup>a</sup>	Study <sup>b</sup>	Study <sup>c</sup>
FWM	916 ± 28	838 ± 18	847 ± 43	699 ± 38
OWM	959 ± 33	832 ± 18	-	758 ± 49
Genu of CC	921 ± 39	-	-	721 ± 68
Splenium of CC	1011 ± 80	-	-	748 ± 64
FGM	1651 ± 157	1322 ± 34	1763 ± 60	1209 ± 109
OGM	1657 ± 99	1283 ± 37	-	1122 ± 117
Caudate	1436 ± 45	-	1483 ± 42	1258 ± 55
Putamen	1332 ± 29	-	1337 ± 42	1102 ± 40
Thalamus	1292 ± 34	-	1218 ± 40	986 ± 33

<sup>a</sup>Wansapura et al. (33)

<sup>b</sup>Gelman et al. (25)

<sup>c</sup>Lu et al. (26)

Table 4. Calculated mean Ratiometric  $R_{ex}$  values ( $\pm$  standard deviation) for white matter, grey matter, and basal ganglia in 5 healthy human volunteers (median age 30). Manual ROIs were placed in 9 different positions defined as white matter (WM: frontal lobe, occipital lobe, corpus callosum), grey matter (GM: frontal lobe, occipital lobe), basal ganglia (caudate, putamen) and thalamus in each volunteer. Location of ROIs is displayed in Figure 4C. Average of ratiometric  $R_{ex}$  was measured within each matched anatomical region in each volunteer. Mixed effects model was tested to calculate statistical significance for ratiometric  $R_{ex}$  differences of each pair of combinations (in total 6 pairs). The only significant difference of the ratiometric  $R_{ex}$  values was found between WM and Thalamus ( $p < 0.05$ ).

		GM	WM	Basal Ganglia	Thalamus
Mean $\pm$ Std of Ratiometric $R_{ex}$		$0.49 \pm 0.02$	$0.48 \pm 0.03$	$0.49 \pm 0.02$	$0.51 \pm 0.01$
Statistical significance (p-value)	WM	0.28	-	0.65	0.02
	Basal Ganglia	0.58	0.65	-	0.08
	Thalamus	0.19	0.02	0.08	-

Table 5. Mean  $\pm$  Std of Ratiometric  $R_{ex}$  in two patients with MS. Manual ROIs were placed in multiple positions defined as normal appearing white matter (NAWM) and MS lesions in each volunteer. Location of five lesion ROIs is displayed in Figure 5A.

Patient 1				Patient 2		
NAWM	Lesion 1	Lesion 2	Lesion 3	NAWM	Lesion 4	Lesion 5
$0.48 \pm 0.02$	$0.56 \pm 0.01$	$0.48 \pm 0.01$	$0.52 \pm 0.01$	$0.49 \pm 0.01$	$0.48 \pm 0.01$	$0.48 \pm 0.01$

## Figure Legends

Figure 1. A simplified diagram of the pulse sequence. First, an initial saturation by WET pulse (water suppression enhanced through  $T_1$  effects) consisting of four RF pulses is employed to achieve effective nulling of the longitudinal water magnetisation. Then, (A) delays (Look-Locker scan) or (B) off-resonance saturation pulses (PRO-QUEST scan) are applied and interleaved with the acquisition of segmented exchange-weighted images. Progressive saturation gives rise to an observable signal reduction in  $M_z$  throughout relaxation.  $t_d$  = the time between the initial saturation pulse and the first readout pulse;  $t_{del}$  = the delay time replacing the CEST saturation pulse;  $t_{sat}$  = the time for the CEST saturation pulse;  $\tau$  = the time between readout pulses with small flip angle  $\theta$ .

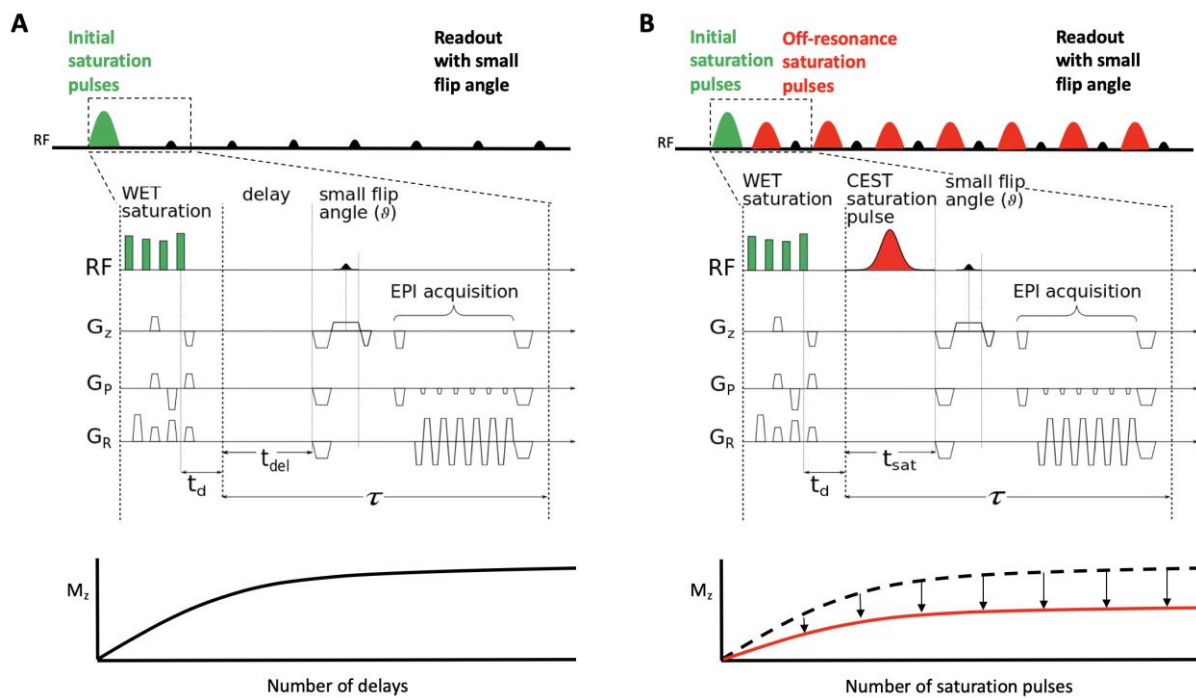


Figure 2. Numerical simulation. Exchange rate ( $k_{ex}$ ) for each flip angle combination was estimated (A) with additive white Gaussian noise. For simulation with the additive noise, the fitting repeated 1000 times with various instances of noise. (B) The standard deviations of 1000 repeated estimates are shown in the log-space. The minimum applicable flip angles that result in an estimate of  $k_{ex} \approx 800$  Hz with small standard deviation are  $300^\circ$  and  $630^\circ$ . (C) Effect of an error  $\Delta T_2$  on  $k_{ex}$  at different magnetic field strengths (3T, 7T and 9.4T).

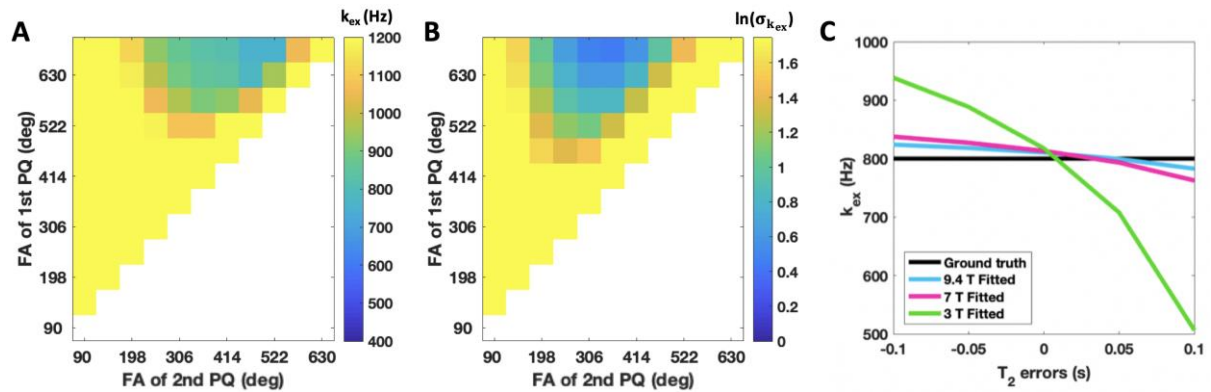


Figure 3. Saturation recovery curves of (A) Look-Locker scan (with delay) and (B) PRO-QUEST scan (with off-resonance saturation pulses) in PBS and glutamate (Glu) samples (100 mM) at pH = 6.08, 6.64 and 7.19, and (C) corresponding images of steady-state saturation recovery curves (at the final phase) in samples. The mean values of both (D) single power  $R_{ex}$  ( $R_{ex,high}$ ) and (E) ratiometric  $R_{ex}$  significantly correlate with pH in glutamate samples (100 mM).

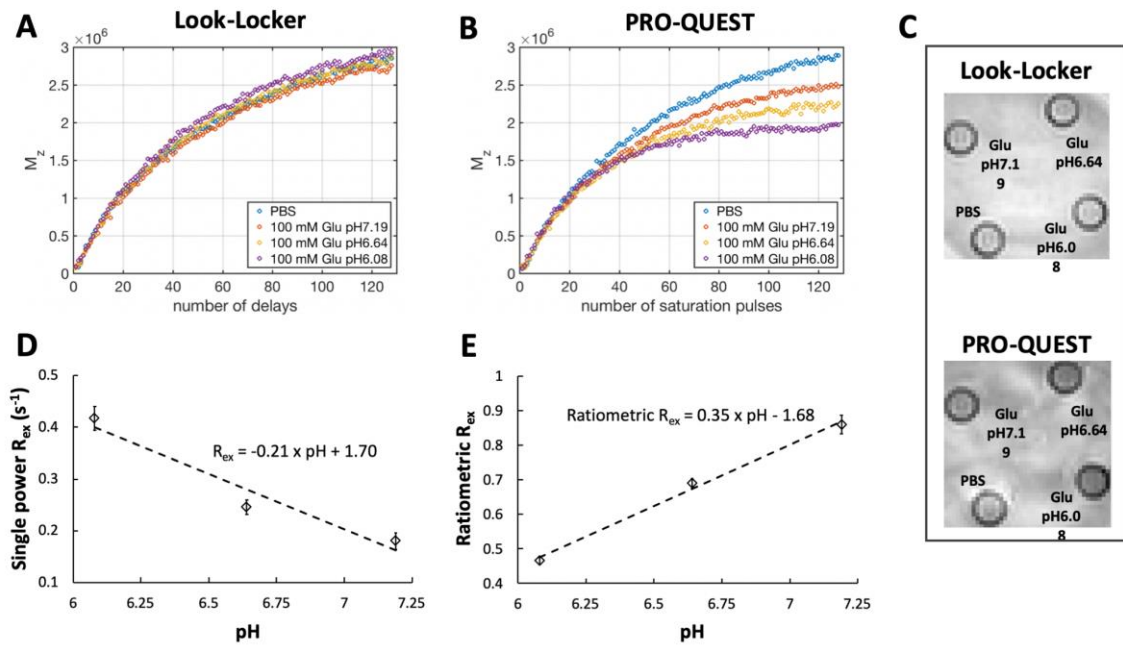


Figure 4. Representative axial brain images of steady-state saturation recovery curves (at the final phase) using (A) Look-Locker sequence (with delay) and (B) PRO-QUEST sequence (with off-resonance saturation pulses) in a healthy volunteer. (C)  $T_1$  map (unit: seconds) for which raw data were obtained from two Look-Locker sequences with small flip angles of  $8^\circ$  and  $15^\circ$ , was computed by maximum likelihood estimation. Saturation recovery curves of (D) Look-Locker scan (with delay), (E) PRO-QUEST scan (with off-resonance saturation pulses) and (F) the  $B_1$  map (in % of the nominal angle) obtained from the same volunteer. Maps of (G)  $R_{ex,low}$  and (H)  $R_{ex,high}$  (unit: 1/seconds) were produced by solving Bloch-McConnell equations with two saturation power setting of PRO-QUEST sequences. (I) A ratiometric  $R_{ex}$  map (unitless) was calculated from  $R_{ex,low}$  divided by  $R_{ex,high}$ , which produces a concentration-independent  $R_{ex}$  (equation 5). In order to exclude extreme ratiometric  $R_{ex}$  originated from CSF compartment, pixels with  $T_1$  over 1780 ms were masked out.

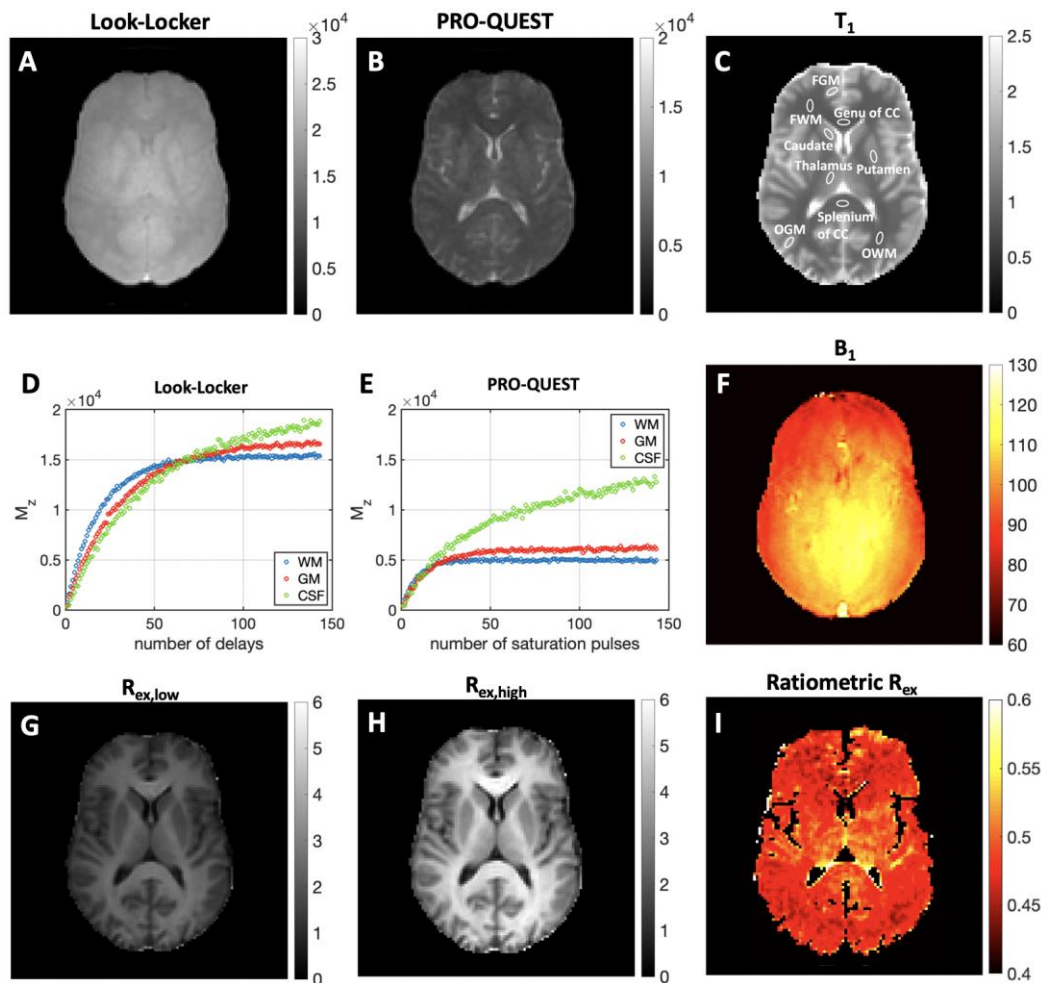
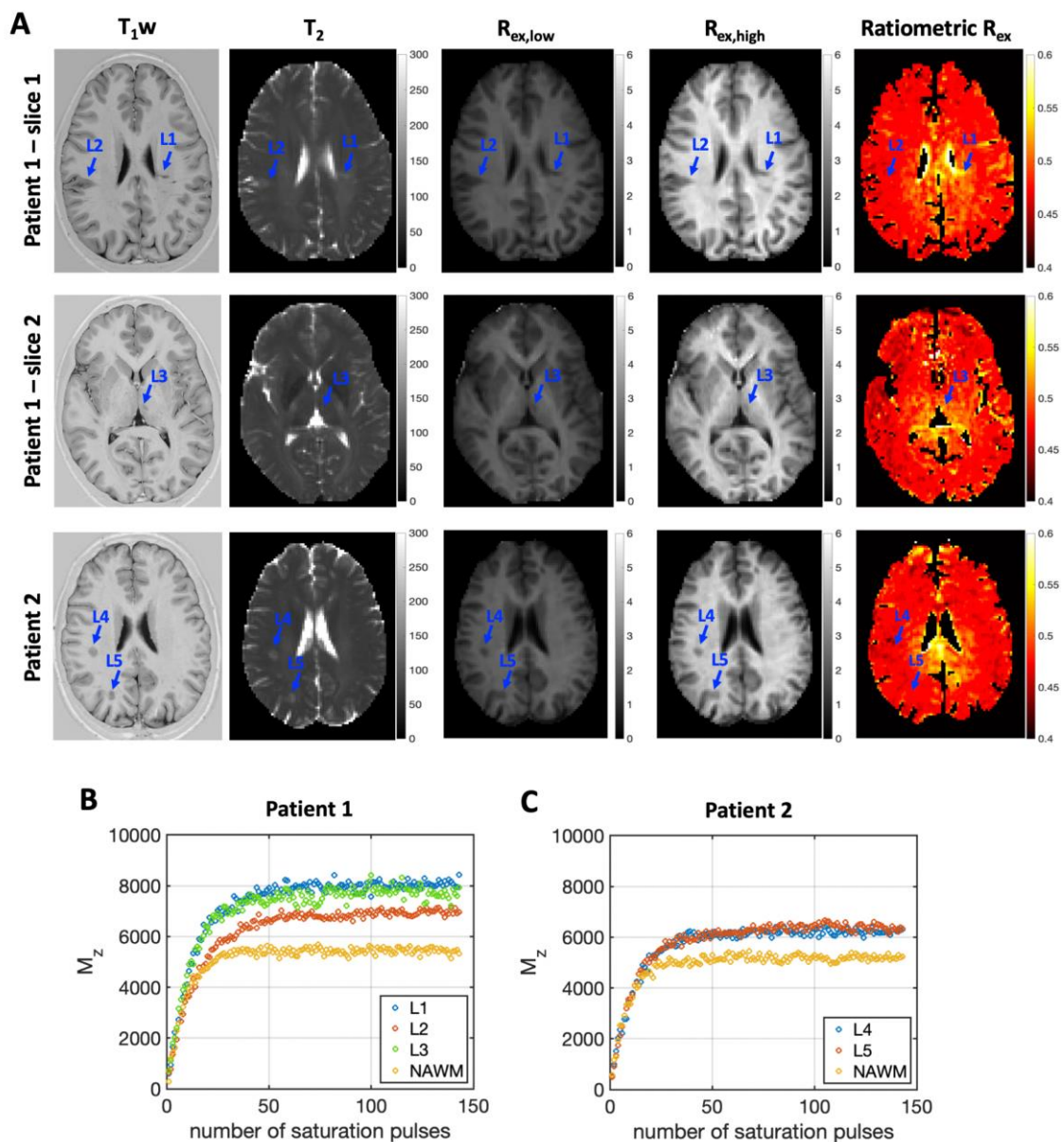
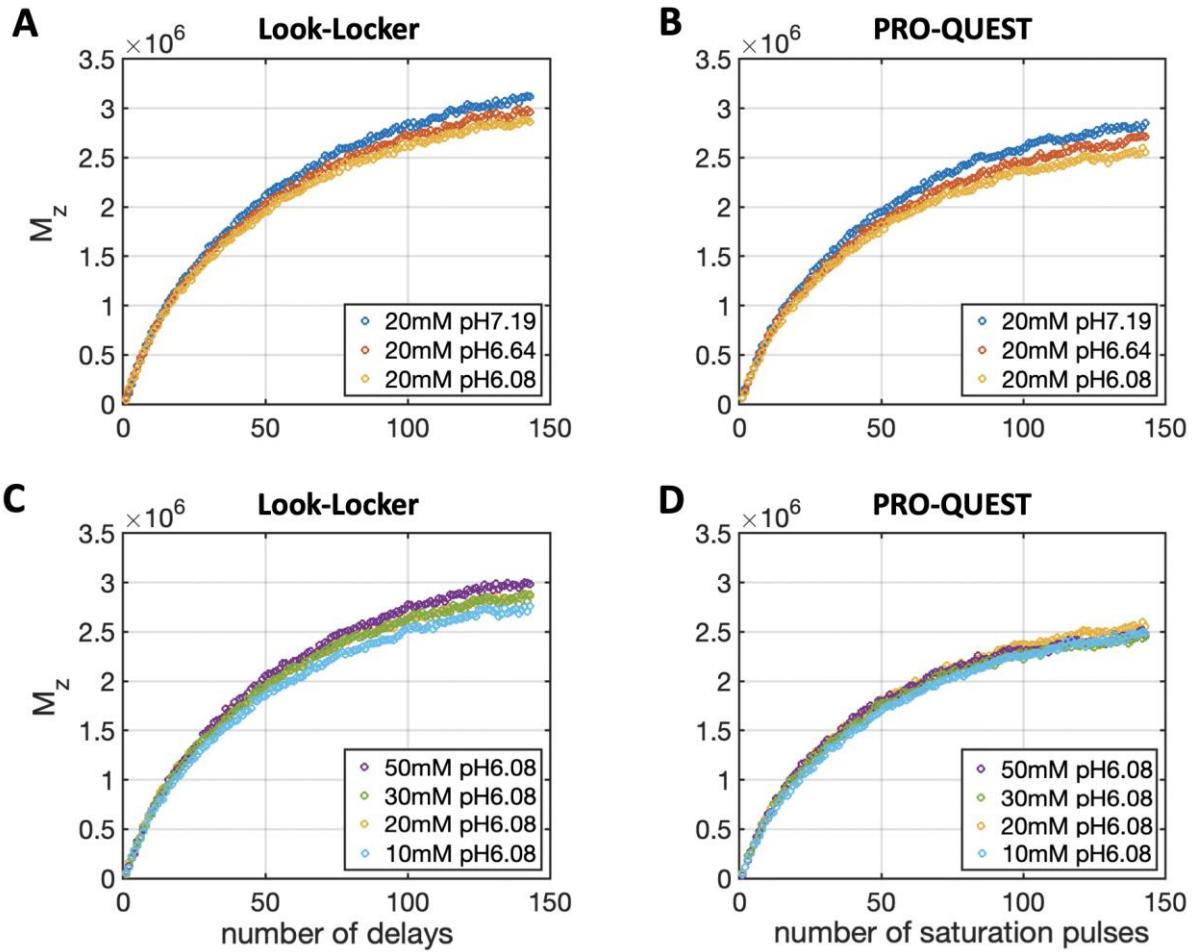


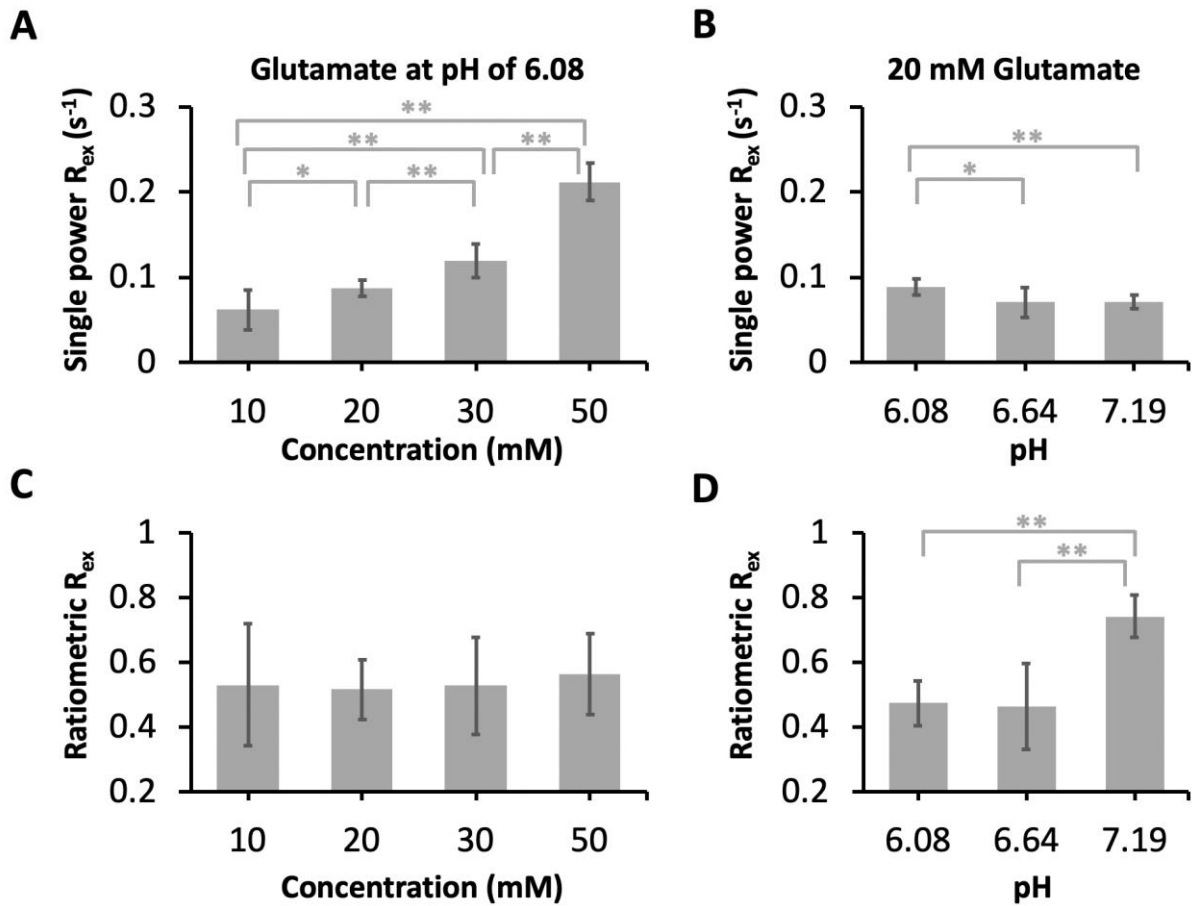
Figure 5. (A) Multiparametric images from two MS patients. From left to right:  $T_1$ w PSIR image, quantitative  $T_2$  (in ms), PRO-QUEST  $R_{ex}$  maps (in Hz) using two saturation power setting ( $R_{ex,low}$  at low saturation power and  $R_{ex,high}$  at high saturation power), ratiometric  $R_{ex}$  (the ratio of two  $R_{ex}$  maps, unitless). MS lesions are indicated by blue arrows L1 – L5 as a reference for Table 5. In order to exclude extreme ratiometric  $R_{ex}$  originated from CSF compartment, pixels with  $T_1$  over 1780 ms were masked out. Saturation recovery curves of PRO-QUEST scan (with off-resonance saturation pulses) obtained from MS lesions (L1 - L5) and NAWM from the (B) patient 1 and (C) patient 2.



Supporting Information Figure S1. Saturation recovery curves of (A, C) Look-Locker scan (with delay) and (B, D) PRO-QUEST scan (with off-resonance saturation pulses) in glutamate samples. (A, B) At various pH with a fixed concentration of glutamate samples (20 mM). (C, D) Various concentration of glutamate samples at a fixed pH of 6.08.



Supporting Information Figure S2. Mean values of (A) single power  $R_{ex}$  ( $R_{ex,high}$ ) and (C) ratiometric  $R_{ex}$  at various concentration of glutamate samples with a fixed pH of 6.08, and mean values of (B) single power  $R_{ex}$  ( $R_{ex,high}$ ) and (D) ratiometric  $R_{ex}$  at various pH of glutamate samples with a fixed concentration (20 mM). The error bar represents the standard deviation. Significant differences between groups are indicated by \* $p < 0.05$  and \*\* $p < 0.001$ .



Supporting Information: *Derivation of PRO-QUEST and Look-Locker equations*

For efficient description of derivations, we firstly outline the derivation of equation 3 followed by equation 1. All timings are shown on the sequence diagram (Figure 1). The initial magnetization is  $M(t = 0) = 0$ , assuming perfect initial and instantaneous saturation. The time  $t_d$  passes until the beginning of the first CEST saturation pulse. During this time, the magnetisation  $M$  recovers with  $R_1$  towards equilibrium magnetization  $M_0$ . Hence, at  $t_d$  (the time between the initial saturation pulse and the first readout pulse), the magnetisation is given by:

$$M(t = t_d) = M_0(1 - e^{-t_d R_1}). \quad [6]$$

During the first CEST saturation pulse, the magnetisation recovers with  $R_{1\rho}$  towards  $M_{ss}$  (the steady-state magnetization). Hence, at the end of the pulse, the magnetisation is given by:

$$M(t = t_d + t_{sat}) = M(t = t_d) * e^{-t_{sat} R_{1\rho}} + M_{ss}(1 - e^{-t_{sat} R_{1\rho}}) \quad [7]$$

where  $t_{sat}$  is the time for the CEST saturation pulse and  $R_{1\rho}$  is the relaxation constant along the effective field. We assume that the following readout pulse is instantaneous (zero duration). This readout reduces the magnetization by a factor  $\cos\theta$ :

$$M(t = t_d + t_{sat}) \rightarrow M(t = t_d + t_{sat})(\cos\theta) \quad [8]$$

During the inter-pulse delay of the module, i.e., until time  $t = t_d + t_{sat} + (\tau - t_{sat}) = t_d + \tau$ , no pulse is played, therefore the magnetisation recovers with  $R_1$  towards  $M_0$ :

$$M(t = t_d + \tau) = M(t = t_d + t_{sat})e^{-(\tau - t_{sat})R_1} + M_0(1 - e^{-(\tau - t_{sat})R_1}) \quad [9]$$

where  $\tau$  is the time between readout pulses with small flip angle  $\theta$ . Repeating this scheme for further CEST-pulse inter-pulse delay modules leads to the following general formula for the magnetization at the  $N$ th readout:

$$M(t = t_d + (N - 1) * \tau + t_{sat}) = [M(t_d)e^{-t_{sat}R_{1\rho}} + M_{ss}(1 - e^{-t_{sat}R_{1\rho}})]\epsilon^{N-1} + [M_{ss}(1 - e^{-t_{sat}R_{1\rho}}) + M_0(1 - e^{-(\tau - t_{sat})R_1})e^{-t_{sat}R_{1\rho}}](\epsilon^{N-2} + \epsilon^{N-3} + \dots + \epsilon^1 + \epsilon^0) \quad [10]$$

where  $(\cos\theta)e^{-(\tau - t_{sat})R_1}e^{-t_{sat}R_{1\rho}}$  term is replaced by  $\epsilon$ .

Using the geometric sum formula for the last expression this can be rewritten as:

$$M(t = t_d + (N - 1)\tau + t_{sat}) = [M(t_d)e^{-t_{sat}R_{1\rho}} + M_{ss} * (1 - e^{-t_{sat}R_{1\rho}})]\epsilon^{N-1} + [M_{ss}(1 - e^{-t_{sat}R_{1\rho}}) + M_0(1 - e^{-(\tau - t_{sat})R_1})e^{-t_{sat}R_{1\rho}}] \frac{1 - \epsilon^{N-1}}{1 - \epsilon} \quad [11]$$

Replacing  $\epsilon$  with  $(\cos\theta)e^{-(\tau - t_{sat})R_1}e^{-t_{sat}R_{1\rho}}$ , equation 3 is obtained.

$$\begin{aligned}
M(t = t_d + (N - 1)\tau + t_{\text{sat}}) &= [M_0(1 - e^{-t_d R_1})e^{-t_{\text{sat}} R_1 \rho} + M_{\text{SS}}(1 - e^{-t_{\text{sat}} R_1 \rho})]((\cos\theta)e^{-t_{\text{sat}} R_1 \rho} e^{-(\tau - t_{\text{sat}}) R_1})^{(N-1)} \\
&+ M_{\text{Zsat}}(\tau) \left( \frac{1 - ((\cos\theta)e^{-t_{\text{sat}} R_1 \rho} e^{-(\tau - t_{\text{sat}}) R_1})^{(N-1)}}{1 - ((\cos\theta)e^{-t_{\text{sat}} R_1 \rho} e^{-(\tau - t_{\text{sat}}) R_1})} \right)
\end{aligned} \tag{3}$$

Next, equation 1 is obtained as a case-limit of equation 3 for:

$$\begin{aligned}
R_{1\rho} &\rightarrow R_1 \\
M_{\text{SS}} &\rightarrow M_0 \\
t_{\text{sat}} &\rightarrow t_{\text{del}}
\end{aligned}$$

These variable replacements account for the lack of a saturation pulse during the time interval  $t_{\text{del}}$ .

Hence, we obtain:

$$\begin{aligned}
M(t = t_d + (N - 1)\tau + t_{\text{del}}) &= [M(t_d)e^{-t_{\text{del}} R_1} + M_0(1 - e^{-t_{\text{del}} R_1})]\epsilon^{N-1} + [M_0(1 - e^{-t_{\text{del}} R_1}) + \\
&M_0(1 - e^{-(\tau - t_{\text{del}}) R_1})e^{-t_{\text{del}} R_1}] \frac{1 - \epsilon^{N-1}}{1 - \epsilon}
\end{aligned} \tag{12}$$

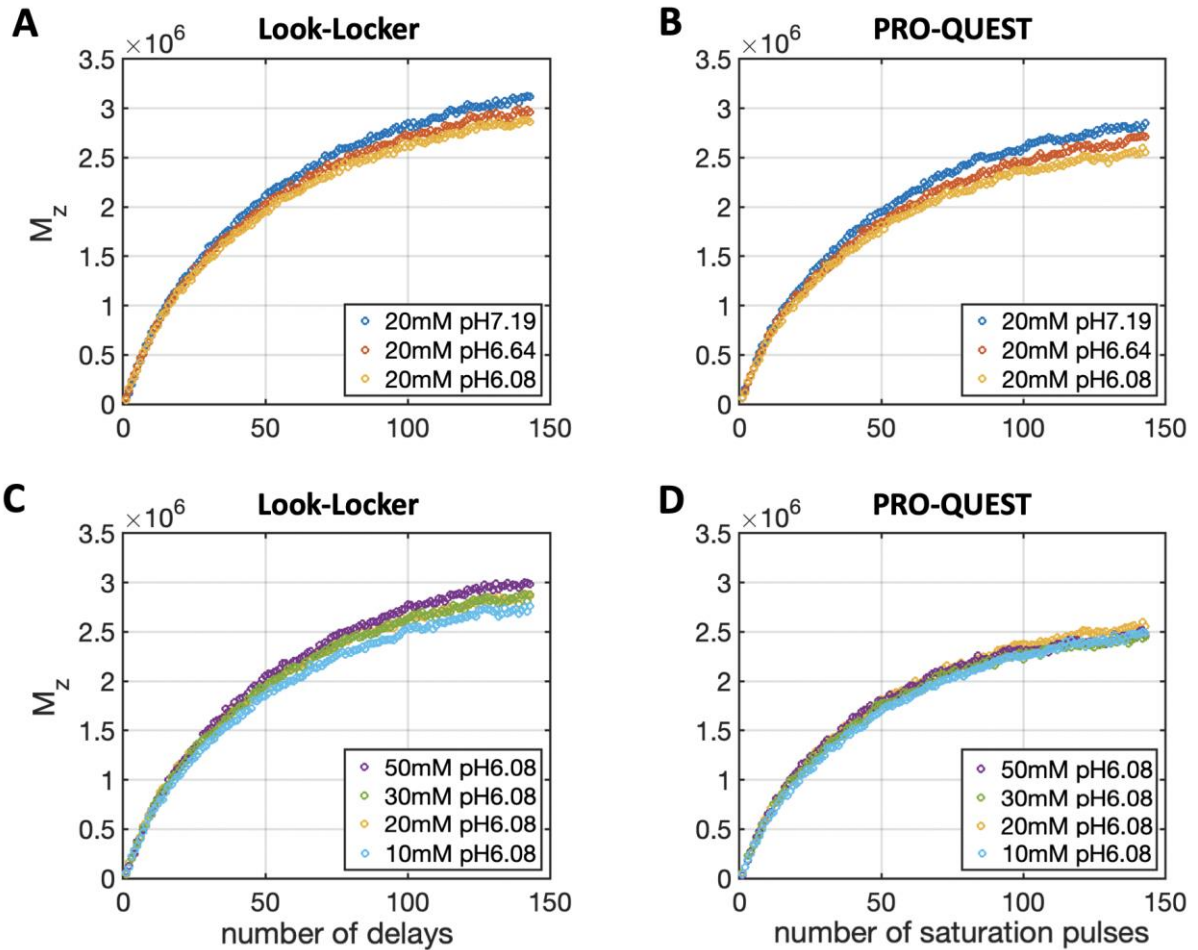
This can be simplified to:

$$M(t = t_d + (N - 1)\tau + t_{\text{del}}) = [M(t_d)e^{-t_{\text{del}} R_1} + M_0(1 - e^{-t_{\text{del}} R_1})]\epsilon^{N-1} + M_0(1 - e^{-\tau R_1}) \frac{1 - \epsilon^{N-1}}{1 - \epsilon} \tag{13}$$

Replacing  $\epsilon$  with  $(\cos\theta)e^{-(\tau - t_{\text{sat}}) R_1} e^{-t_{\text{sat}} R_1 \rho}$ , equation 1 is obtained.

$$M(t = t_d + (N - 1)\tau + t_{\text{del}}) = [M_0(1 - e^{-t_d R_1})e^{-t_{\text{del}} R_1} + M_0(1 - e^{-t_{\text{del}} R_1})]((\cos\theta)e^{-\tau R_1})^{N-1} + M_{\text{Zd}}(\tau) \frac{1 - ((\cos\theta)e^{-\tau R_1})^{(N-1)}}{1 - ((\cos\theta)e^{-\tau R_1})} \tag{1}$$

Supporting Information Figure S1. Saturation recovery curves of (A, C) Look-Locker scan (with delay) and (B, D) PRO-QUEST scan (with off-resonance saturation pulses) in glutamate samples. (A, B) At various pH with a fixed concentration of glutamate samples (20 mM). (C, D) Various concentration of glutamate samples at a fixed pH of 6.08.



Supporting Information Figure S2. Mean values of (A) single power  $R_{ex}$  ( $R_{ex,high}$ ) and (C) ratiometric  $R_{ex}$  at various concentration of glutamate samples with a fixed pH of 6.08, and mean values of (B) single power  $R_{ex}$  ( $R_{ex,high}$ ) and (D) ratiometric  $R_{ex}$  at various pH of glutamate samples with a fixed concentration (20 mM). The error bar represents the standard deviation. Significant differences between groups are indicated by \* $p < 0.05$  and \*\* $p < 0.001$ .

